

# Analytical description of inverse filter emulating the plasmon injection loss compensation scheme and implementation for ultra-high resolution hyperlens

XU ZHANG,<sup>1</sup> WYATT ADAMS,<sup>1</sup> AND DURDU Ö. GÜNEY<sup>1,\*</sup>

<sup>1</sup>Department of Electrical and Computer Engineering, Michigan Technological University, 1400 Townsend Dr., Houghton, MI 49931-1295, USA

\*Corresponding author: [dgüney@mtu.edu](mailto:dgüney@mtu.edu)

Received XX Month XXXX; revised XX Month, XXXX; accepted XX Month XXXX; posted XX Month XXXX (Doc. ID XXXXX); published XX Month XXXX

**An inverse filter full analytical description and implementation of a recently proposed plasmon injection scheme for improving the resolution of a hyperlens is presented. Different types of loss mechanisms existing in the hyperlens imaging system are identified and studied in detail. It is shown that the plasmon injection scheme and its inverse filter analogue can compensate all the major loss mechanisms. As a result, an object with deep sub-wavelength features, otherwise unresolvable with a hyperlens alone, is fully reconstructed. © 2017 Optical Society of America**

## 1. Introduction

Abbe's diffraction limit generally restricts the resolution of conventional optical systems [1]. Subwavelength features which correspond to rapid spatial variance of electromagnetic waves are decayed exponentially and are consequently too weak to contribute to the image in the far-field. The smallest feature size which conventional optical systems can resolve is about one half of the light wavelength. Engineered at subwavelength scales, metamaterials have enabled unprecedented control of light at both classical and quantum domains [2-18]. Perfect lenses [19-21], superlenses [22-24], flat lenses [25,26], and hyperlenses including magnifying superlenses [27-35] based on metamaterials have been proposed or experimentally demonstrated. A review of superlenses in the general context of near-field optics is provided in Ref. [36]. These lenses provide the possibility to break the diffraction limit. The ability for converting evanescent waves to propagating waves and hence allowing for image processing with conventional optical components has made hyperlenses receive much attention along with alternative approaches such as super-resolution imaging with microsphere lenses [37,38]. So far, the proposed and fabricated hyperlenses mainly consist of pairs of metal and dielectric layers. These structures are highly anisotropic metamaterials with generally opposite signs of permittivity tensor elements to give hyperbolic dispersion.

Unfortunately, different types of loss mechanisms exist which constrain the hyperlens resolution. These loss mechanisms include absorptive loss such as in metal components [39], discretization loss (i.e. periodicity artifacts [40]) arising from the invalidity of the homogeneous effective medium approximation, and impedance mismatch loss which appears at the interface between hyperlens and substrate [41].

Recently, we have proposed a novel loss compensation technique called the plasmon injection scheme (or referred to as  $\Pi$  scheme) [42]. The  $\Pi$  scheme is realized by a coherent superposition of two electromagnetic fields in a lossy medium such as a metamaterial. One of the fields constitutes the signal and is excited in the metamaterial by an

external input field such as an object field to be imaged. The other field is the pump and is excited in the metamaterial by an external auxiliary field. The pump field is used to compensate the photon loss in the signal. Although the original  $\Pi$  scheme [42] was based on surface plasmon polariton (SPP) modes in plasmonic metamaterials [43-45], hence the name, the concept is equally applicable to any type of electromagnetic modes. The key feature that no gain medium is needed makes this technique highly attractive for research. Previously, we have successfully applied the  $\Pi$  scheme to a perfect lens [46] and a hyperlens [47]. We have also demonstrated that the  $\Pi$  scheme loss compensation in these lenses is equivalent to applying a simple spatial filter to the raw image, similar to an inverse or pseudoinverse filter for deconvolution of near-field images [48-52]. In Ref. [47], we used one experimentally realized hyperlens as an example [33] to show the applicability of the  $\Pi$  scheme loss compensation technique, and achieved a resolution of  $\lambda_0/7$ , where  $\lambda_0$  is the free space wavelength. In this paper, we will show the mathematical details of the entire procedure of the  $\Pi$  scheme loss compensation technique as an equivalent inverse filter post-processing scheme and implement it for a hyperlens imaging system to demonstrate that this technique can compensate losses originating from different types of physical mechanisms, not only absorption but also discretization and impedance mismatch.

## 2. Procedure for the inverse filter loss compensation technique emulating the $\Pi$ scheme

The hyperlens we studied in the previous paper [47] and here is from Ref. [33]. It consists of 8 pairs of Ag/Al<sub>2</sub>O<sub>3</sub> layers surrounded by quartz. The layer thickness is 35nm for both Ag and Al<sub>2</sub>O<sub>3</sub>. At experimentally working wavelength  $\lambda_0 = 365nm$ , the relative permittivity of silver, aluminum oxide, and quartz are  $\epsilon_m = -2.4012 + 0.2488i$ ,  $\epsilon_d = 3.217$ , and  $\epsilon_{qtz} = 2.174$ , respectively. This layered structure can be considered as a homogenous anisotropic structure with the effective permittivity satisfying the following equations:

$$\epsilon_p = \frac{\epsilon_m \epsilon_d}{(1-p)\epsilon_m + p\epsilon_d} \quad (1)$$

$$\epsilon_\phi = p\epsilon_m + (1-p)\epsilon_d \quad (2)$$

where  $p$  is the filling ratio of the metal. In this designed structure,  $p = 0.5$ , and then  $\epsilon_p = -16.7786 + 7.0793i$  and  $\epsilon_\phi = 0.4079 + 0.1244i$ .

Fig. 1 shows the geometry of the studied hyperlens. Due to the invariance along the  $z$  axis of symmetry, a two-dimensional model is sufficient to simulate one-dimensional imaging through this hyperlens. The commercial finite element solver COMSOL Multiphysics software is used here. This hyperlens works under transverse-magnetic (TM) polarization excitation. Perfectly matched layers (PML) are added at the boundaries to absorb outgoing waves. All the other simulation details including the object definitions can be found in Ref. [47].

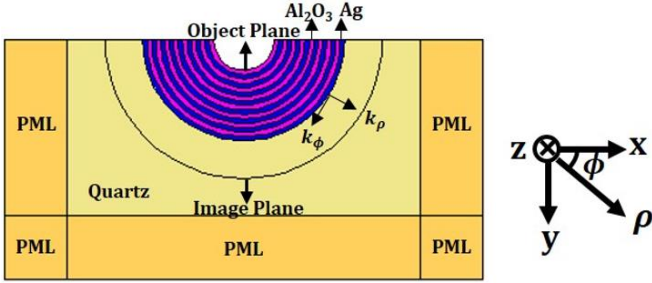


Figure 1. Geometry for the studied hyperlens designed in COMSOL. Cylindrical coordinate system  $(\rho, \phi, z)$  is used in the simulation.

In the following parts, we will show the steps of the loss compensation technique. In section 2.A, we will derive the electromagnetic wave solution for this anisotropic material. In section 2.B, the object plane and image plane are defined. In section 2.C, we will show that an arbitrary electromagnetic field can be expanded in the basis of the mode solutions calculated in section 2.A. Since the  $\Pi$  scheme loss compensation technique is equivalent to applying a compensation filter [42,46,47], which is the inverse of the hyperlens transfer function, the transfer function calculation based on the electromagnetic modes of the hyperlens is shown in section 2.D. Then in section 2.E, the compensation filter is applied to reconstruct the deep sub-diffraction limited image. As a result of a fixed object and image plane, the loss compensation technique can be simplified, which will be proved in section 2.F. In section 2.G, the cut off frequency of the transfer function due to the numerical error is determined. In sections 3.A, 3.B, and 3.C, we show through the implementations of the  $\Pi$  scheme that it is capable of compensating all the major loss mechanisms in the hyperlens imaging system including absorption, discretization, and impedance mismatch losses, respectively. Finally, we will discuss the magnifying superlens [34,35] in the context of the  $\Pi$  scheme and conclude in section 4.

#### A. Mode solution in hyperlens

Here we assume TM polarization (i.e., field components  $E_\rho$ ,  $E_\phi$ , and  $H_z$ )

and the permittivity tensor  $\bar{\epsilon}_r = \begin{bmatrix} \epsilon_\rho & 0 & 0 \\ 0 & \epsilon_\phi & 0 \\ 0 & 0 & \epsilon_z \end{bmatrix}$ . In cylindrical

coordinates, the time-harmonic form of Maxwell equations  $\nabla \times \vec{H} = -j\omega\vec{D}$  and  $\nabla \times \vec{E} = j\omega\vec{B}$  can be written as:

$$\nabla \times \vec{H} = \frac{1}{\rho} \begin{vmatrix} \hat{\rho} & \rho\hat{\phi} & \hat{z} \\ \frac{\partial}{\partial \rho} & \frac{\partial}{\partial \phi} & 0 \\ 0 & 0 & H_z \end{vmatrix} = \frac{1}{\rho} \frac{\partial H_z}{\partial \phi} \hat{\rho} - \frac{\partial H_z}{\partial \rho} \hat{\phi} \quad (3)$$

$$\nabla \times \vec{E} = \frac{1}{\rho} \begin{vmatrix} \hat{\rho} & \rho\hat{\phi} & \hat{z} \\ \frac{\partial}{\partial \rho} & \frac{\partial}{\partial \phi} & 0 \\ E_\rho & \rho E_\phi & 0 \end{vmatrix} = \frac{1}{\rho} \left[ \frac{\partial(\rho E_\phi)}{\partial \rho} - \frac{\partial E_\rho}{\partial \phi} \right] \hat{z} \quad (4)$$

$$j\omega\vec{D} = j\omega\epsilon_0\bar{\epsilon}_r\vec{E} = j\omega\epsilon_0 \begin{bmatrix} \epsilon_\rho & 0 & 0 \\ 0 & \epsilon_\phi & 0 \\ 0 & 0 & \epsilon_z \end{bmatrix} \begin{bmatrix} E_\rho \\ E_\phi \\ 0 \end{bmatrix} = j\omega\epsilon_0(\epsilon_\rho E_\rho \hat{\rho} + \epsilon_\phi E_\phi \hat{\phi}) \quad (5)$$

$$j\omega\vec{B} = j\omega\mu_0\mu_r\vec{H} = j\omega\mu_0 H_z \hat{z} \quad (6)$$

Thus, we obtain three coupled equations corresponding to  $\rho$ ,  $\phi$ ,  $z$  components, respectively:

$$\begin{cases} j\omega\epsilon_0\epsilon_\rho E_\rho = -\frac{1}{\rho} \frac{\partial H_z}{\partial \phi} \\ j\omega\epsilon_0\epsilon_\phi E_\phi = \frac{\partial H_z}{\partial \rho} \\ \frac{1}{\rho} \left[ \frac{\partial(\rho E_\phi)}{\partial \rho} - \frac{\partial E_\rho}{\partial \phi} \right] = j\omega\mu_0 H_z \end{cases} \quad (7)$$

Eliminating  $E_\rho$  and  $E_\phi$  in Eq. (7) and using the free space relations  $c = 1/\sqrt{\epsilon_0\mu_0}$ ,  $k_0 = 2\pi/\lambda_0 = 2\pi/(c/f) = \omega/c$ , we obtain Eq. (8) which only contains the  $H_z$  component:

$$\frac{\rho}{\epsilon_\phi} \frac{\partial}{\partial \rho} \left( \rho \frac{\partial H_z}{\partial \rho} \right) + \frac{1}{\epsilon_\rho} \frac{\partial^2 H_z}{\partial \phi^2} = -k_0^2 \rho^2 H_z \quad (8)$$

Using the separation-of-variables method [53], the solution can be written in the form of:

$$H_z = R(\rho)\Phi(\phi) \quad (9)$$

Substituting Eq. (9) into Eq. (8), we obtain:

$$\frac{1}{\epsilon_\phi} \frac{\rho}{R(\rho)} \frac{d}{d\rho} \left( \rho \frac{dR(\rho)}{d\rho} \right) + \frac{1}{\epsilon_\rho} \frac{1}{\Phi(\phi)} \frac{d^2 \Phi(\phi)}{d\phi^2} = -k_0^2 \rho^2 \quad (10)$$

Since the second term in Eq. (10) is a function of only  $\phi$  component, it can be set equal to a constant:

$$\frac{1}{\Phi(\phi)} \frac{d^2 \Phi(\phi)}{d\phi^2} = -m^2 \quad (11)$$

The valid solution for  $\Phi(\phi)$  is:

$$\Phi(\phi) \propto e^{im\phi} \quad (12)$$

Substituting Eq. (11) into Eq. (10), for  $\rho$  component,  $R(\rho)$  satisfies:

$$\rho^2 \frac{d^2 R(\rho)}{d\rho^2} + \rho \frac{dR(\rho)}{d\rho} + \left( \rho^2 k_0^2 \varepsilon_\phi - \frac{\varepsilon_\phi}{\varepsilon_\rho} m^2 \right) R(\rho) = 0 \quad (13)$$

Eq. (13) is a generalized Bessel equation, the solution has the form:

$$R(\rho) \propto J_m \sqrt{\frac{\varepsilon_\phi}{\varepsilon_\rho}} (k_0 \sqrt{\varepsilon_\phi} \rho) \quad (14)$$

Therefore, the final solution can be written as a product of  $R(\rho)$  and  $\Phi(\phi)$ :

$$H_z(\rho, \phi) \propto J_m \sqrt{\frac{\varepsilon_\phi}{\varepsilon_\rho}} (k_0 \sqrt{\varepsilon_\phi} \rho) e^{im\phi} \quad (15)$$

Here  $m$  is the angular momentum mode number of the cylindrical wave. Due to the angular momentum conservation, the tangential component of the wave vector  $k_\phi$  satisfies the equation  $m = k_\phi \rho$ , where  $\rho$  is the distance from center.

Since the real parts of  $\varepsilon_\phi$  and  $\varepsilon_\rho$  have opposite signs and are considerably larger in magnitude than the imaginary parts, the hyperlens has hyperbolic dispersion relation, which has approximately the form [27,54,55]:

$$\frac{k_\rho^2}{\varepsilon_\phi} - \frac{k_\phi^2}{|\varepsilon_\rho|} = \left( \frac{\omega}{c} \right)^2 \quad (16)$$

With the wave propagating away from the center,  $k_\phi$  is decreased as a result of increasing  $\rho$ . Meanwhile, the image is magnified by approximately a factor of  $(r_2/r_1)$ , where  $r_1$  and  $r_2$  are the radii of the object and image planes, respectively.

## B. Selection of the object and image planes

Due to the cylindrical coordinate system, the object and image surfaces are curved as shown in Fig. 1. We prefer to call these surfaces in the rest of the paper as the “object plane” and “image plane,” respectively, since the object and image are still confined to quasi-planar edges of the hyperlens in most experiments [29-33]. The object plane is selected as the inner surface of the hyperlens. The radius of the object plane is  $r_1 = 240nm$ . Imaging with the hyperlens differs from the negative index flat lens [46], in that the distance between the image plane and object plane for the flat lens is equal to twice the lens thickness, resulting in an automatic phase compensation at the image plane [19]. However, in the hyperlens, for different spatial frequency  $k_\phi$ , the phase is restored at different positions. Since there is no unique image plane to realize the phase compensation, we can arbitrarily choose the image plane location. This means that the compensation scheme should then account for both the amplitude and phase. The radius of the image plane we choose here is  $r_2 = 1100nm$ . As a result, the image has around 4.5 times magnification.

## C. Cylindrical wave expansion of an arbitrary electromagnetic field

### 1. Expansion at the object plane

An object here can be represented by a TM polarized arbitrary magnetic field  $O_z(\rho, \phi)$ , which can be expanded in a basis of cylindrical waves obtained in section 2.A:

$$O_z(\rho, \phi) = \quad (17)$$

$$\int_0^{+\infty} \sum_{m=0}^{+\infty} A(k_\rho, m) \cdot J_m \sqrt{\frac{\varepsilon_\phi}{\varepsilon_\rho}} (k_0 \sqrt{\varepsilon_\phi} \rho) e^{im\phi} k_\rho dk_\rho$$

where,

$$A(k_\rho, m) = \tilde{F}(O_z(\rho, \phi)) = \int_0^{+\infty} \int_0^{2\pi} O_z(\rho, \phi) [J_m \sqrt{\frac{\varepsilon_\phi}{\varepsilon_\rho}} (k_0 \sqrt{\varepsilon_\phi} \rho)]^* e^{-im\phi} \rho d\rho d\phi \quad (18)$$

The object is defined at the object plane  $\rho = r_1$ , and  $k_\rho$  is related to  $m$  by Eq. (16). Thus, Eq. (17) can be written as:

$$\begin{aligned} O_z(\rho = r_1, \phi) &= \sum_{m=0}^{+\infty} A(k_\rho(m, \rho = r_1), m) \cdot J_m \sqrt{\frac{\varepsilon_\phi}{\varepsilon_\rho}} (k_0 \sqrt{\varepsilon_\phi} r_1) e^{im\phi} k_\rho(m, \rho = r_1) \\ &= \sum_{m=0}^{+\infty} A(k_{\rho 1}(m), m) B(m) k_{\rho 1}(m) e^{im\phi} \end{aligned} \quad (19)$$

where we define:

$$J_m \sqrt{\frac{\varepsilon_\phi}{\varepsilon_\rho}} (k_0 \sqrt{\varepsilon_\phi} r_1) = B(m) \quad (20)$$

Then Eq. (18) changes to:

$$\begin{aligned} A(k_{\rho 1}(m), m) &= \tilde{F}(O_z(\rho = r_1, \phi)) \\ &= \tilde{O}(m) \\ &= \sum_{n=0}^{+\infty} O_z(\rho = r_1, \phi_n) \cdot \left[ J_m \sqrt{\frac{\varepsilon_\phi}{\varepsilon_\rho}} (k_0 \sqrt{\varepsilon_\phi} r_1) \right]^* e^{-im\phi_n r_1} \\ &= B^*(m) r_1 \sum_{n=0}^{+\infty} O_z(\rho = r_1, \phi_n) e^{-im\phi_n} \end{aligned} \quad (21)$$

Then we obtain:

$$\begin{aligned} \tilde{F}(O_z(\rho = r_1, \phi)) &= \\ \tilde{F}_\rho(O_z(\rho = r_1, \phi)) \tilde{F}_\phi(O_z(\rho = r_1, \phi)) \end{aligned} \quad (22)$$

The  $\rho$  part  $\tilde{F}_\rho(O_z(\rho = r_1, \phi)) = B^*(m) r_1$ , is constant for different  $m$  and can be easily calculated. On the other hand, the  $\phi$  part can be calculated in MATLAB:

$$\begin{aligned} \tilde{O}'(m) &= \tilde{F}_\phi(O_z(\rho = r_1, \phi)) \\ &= \sum_{n=0}^{+\infty} O_z(\rho = r_1, \phi_n) e^{-im\phi_n} \end{aligned} \quad (23)$$

and then:

$$\tilde{O}(m) = B^*(m)r_1\tilde{O}'(m) \quad (24)$$

## 2. Expansion at the image plane

Similar to the object, the raw image  $I_z(\rho, \phi)$  obtained at the image plane  $\rho = r_2$  satisfies the following equations:

$$\begin{aligned} I_z(\rho = r_2, \phi) \\ = \sum_{m=0}^{+\infty} C(k_{\rho 2}(m), m) D(m) k_{\rho 2}(m) e^{im\phi} \end{aligned} \quad (25)$$

$$J_m \sqrt{\frac{\epsilon_\phi}{\epsilon_\rho}} (k_0 \sqrt{\epsilon_\phi} r_2) = D(m) \quad (26)$$

$$\begin{aligned} C(k_{\rho 2}(m), m) = \tilde{I}(m) = D^*(m)r_2 \\ \cdot \sum_{n=0}^{+\infty} I_z(\rho = r_2, \phi_n) e^{-im\phi_n} \end{aligned} \quad (27)$$

$$\tilde{I}'(m) = \sum_{n=0}^{+\infty} I_z(\rho = r_2, \phi_n) e^{-im\phi_n} \quad (28)$$

$$\tilde{I}(m) = D^*(m)r_2\tilde{I}'(m) \quad (29)$$

$\tilde{I}(m)$  and  $\tilde{O}(m)$  are related by the transfer function  $T(m)$  as:

$$\tilde{I}(m) = \tilde{O}(m) T(m) \quad (30)$$

## 3. Increasing the lengths of the object and image planes

The method used in MATLAB to calculate the discrete Fourier transform is the fast Fourier transform. Using the raw image, for example, Eq. (28) is changed to:

$$\begin{aligned} \tilde{I}'(m) = \sum_{n=1}^N I_z(\rho = r_2, \phi_n) \\ \cdot e^{-\frac{i2\pi(m-1)(n-1)}{N}} \end{aligned} \quad (31)$$

Comparing Eq. (31) with Eq. (28), it can be seen that  $\phi_n$  satisfies:

$$\phi_n = \frac{2\pi(n-1)}{N} \quad (32)$$

Eq. (32) requires that the arc length of the image plane should be  $2\pi r_2$ . In the simulation, we can only define  $\phi$  from 0 to  $\pi$ , due to the actual geometry of the fabricated structure. Therefore, a window function is applied to define the fields in the ranges  $\pi < \phi \leq 1.5\pi$  and  $-0.5\pi \leq \phi < 0$ . Since the object is always defined at the central part of the object plane, the corresponding image is also obtained in the center. Hence, we choose a simple rectangular window function  $u(0 \leq \phi \leq \pi) = 1$ , and  $u(-0.5\pi \leq \phi < 0) = u(\pi < \phi \leq 1.5\pi) = 0$ . As a result, the electromagnetic fields outside the computational domain are set to 0.

## D. Transfer function calculation

In the simulation, we define cylindrical waves as the input with the form  $e^{im\phi}$  at the object plane  $\rho = r_1$ , where different  $m$ 's correspond to different spatial frequencies. At the image plane,  $\rho = r_2$ , the complex field information of the image is obtained. We collect the complex magnetic field  $h_o(m)$  at point  $P_1(r_1, \phi_0)$  on the object plane and  $h_i(m)$

at point  $P_2(r_2, \phi_0)$  on the image plane. The angle  $\phi_0$  is arbitrary and chosen  $\pi/2$  for convenience. Then we obtain complex  $T'(m)$ :

$$T'(m) = h_i(m) / h_o(m) \quad (33)$$

Here, we should note that,  $T'(m)$  is not equal to the transfer function  $T(m)$  in Eq. (30). Even in the absence of losses, the cylindrical wave amplitude changes as the wave propagates.  $T'(m)$  is calculated by the division of the fields at the two points. Thus,  $T'(m)$  accounts for only the amplitude change between the object plane and image plane for individual cylindrical waves. In contrast,  $T(m)$  in Eq. (30) results from all the points and waves contributing to the object and image. For example, in the lossless case,  $T(m) = 1$ . Therefore,  $T(m)$  and  $T'(m)$  can be related by:

$$T(m) = T'(m) / t(m) \quad (34)$$

where  $t(m)$  corrects the amplitude change between the image plane and the object plane. For a particular  $m$ , every radial frequency  $k_\rho$  along the curve contributes to the cylindrical wave amplitude. So  $t(m)$  satisfies:

$$\begin{aligned} t(m) \\ = \frac{\int_0^{+\infty} J_m \sqrt{\frac{\epsilon_\phi}{\epsilon_\rho}} (k_0 \sqrt{\epsilon_\phi} \rho) e^{im\phi} k_\rho dk_\rho \Big|_{\rho=r_2}}{\int_0^{+\infty} J_m \sqrt{\frac{\epsilon_\phi}{\epsilon_\rho}} (k_0 \sqrt{\epsilon_\phi} \rho) e^{im\phi} k_\rho dk_\rho \Big|_{\rho=r_1}} \\ = \frac{D(m)k_{\rho 2}(m)}{B(m)k_{\rho 1}(m)} \end{aligned} \quad (35)$$

## E. Loss compensation procedure

Due to losses during the imaging process, the high spatial frequency components of the object which correspond to large  $m$  value are decayed rapidly such that they become too weak to contribute to the image resolution. Therefore, the compensation filter  $F(m) = 1/T(m)$  is used to amplify those frequency components, and the Fourier spectrum of the compensated image  $\tilde{I}_c(m)$  satisfies:

$$\begin{aligned} \tilde{I}_c(m) = \tilde{I}(m)F(m) = \frac{\tilde{O}(m)T(m)}{T(m)} \\ = \tilde{O}(m) \end{aligned} \quad (36)$$

We have shown previously that this inverse filter post-processing is equivalent to physical implementation of the  $\Pi$  scheme with external auxiliary sources [42,46,47].

## F. Simplification of the post-processing procedure for the loss compensation

Since  $\rho$  is fixed at the object and image planes, the Fourier spectrum of the  $\rho$  components is always constant with a fixed  $m$  value. Thus, it can be shown that in order to simplify the post-processing for the loss compensation, we do not need to consider the  $\rho$  components in the calculation. To achieve our goal, first, we will derive two equations below. In section 2.D, we define the object to be  $e^{im\phi}$ , which can be expanded using Eqs. (19) and (21):

$$e^{im\phi} = \sum_{m'=0}^{+\infty} A(k_{\rho 1}(m'), m') B(m') k_{\rho 1}(m') e^{im'\phi} \quad (37)$$

$$A(k_{\rho 1}(m'), m') = B^*(m') r_1 \sum_{n=0}^{+\infty} e^{im\phi_n} \cdot e^{-im'\phi_n} = B^*(m') r_1 \delta(m - m') \quad (38)$$

Substituting  $A(k_{\rho 1}(m'), m')$  into Eq. (37), we obtain:

$$e^{im\phi} = r_1 k_{\rho 1}(m) |B(m)|^2 e^{im\phi} \quad (39)$$

Hence, this gives the first equation:

$$r_1 k_{\rho 1}(m) |B(m)|^2 = 1 \quad (40)$$

Similar to the object plane, at the image plane  $\rho = r_2$ , we can derive another equation:

$$r_2 k_{\rho 2}(m) |D(m)|^2 = 1 \quad (41)$$

Then we define a new compensation filter  $F'(m) = 1/T'(m)$ , which is different from  $F(m) = 1/T(m)$ . Applying  $F'(m)$  directly to  $\tilde{I}'(m)$ , we obtain  $\tilde{I}'_c(m)$ , which is the  $\phi$  component of the Fourier spectrum for the compensated image:

$$\tilde{I}'_c(m) = \tilde{I}'(m) F'(m) = \tilde{I}'(m) / T'(m) \quad (42)$$

Using Eqs. (24), (29), (30), (34), (35), (40), and (41):

$$\begin{aligned} \tilde{I}'_c(m) &= \frac{\tilde{I}'(m)}{T_m t_m} = \frac{\tilde{I}'(m)}{(\frac{\tilde{I}(m)}{\tilde{O}(m)}) (\frac{D(m) k_{\rho 2}(m)}{B(m) k_{\rho 1}(m)})} \\ &= \frac{\tilde{I}(m)}{D^*(m) r_2} \frac{\tilde{O}(m) B(m) k_{\rho 1}(m)}{\tilde{I}(m) D(m) k_{\rho 2}(m)} \\ &= \frac{\tilde{O}(m)}{B^*(m) r_1 r_2 k_{\rho 2}(m) |D(m)|^2} = \tilde{O}'(m) \end{aligned} \quad (43)$$

Thus, the  $\phi$  component of the Fourier spectrum is fully compensated. At the image plane  $\rho = r_2$ , based on Eq. (29),  $\rho$  component of the Fourier spectrum is equal to  $D^*(m) r_2$ . Then,  $\tilde{I}'_c(m)$  is given by:

$$\tilde{I}'_c(m) = D^*(m) r_2 \tilde{I}'_c(m) \quad (44)$$

Taking the inverse Fourier transform:

$$\begin{aligned} I_c(\rho = r_2, \phi) &= \tilde{F}^{-1}(\tilde{I}'_c(m)) \\ &= \sum_{m=0}^{+\infty} \tilde{I}'_c(m) D(m) k_{\rho 2}(m) e^{im\phi} \\ &= \sum_{m=0}^{+\infty} D^*(m) r_2 \tilde{I}'_c(m) D(m) k_{\rho 2}(m) e^{im\phi} \\ &= \sum_{m=0}^{+\infty} \tilde{I}'_c(m) e^{im\phi} \end{aligned} \quad (45)$$

Eq. (45) shows that the inverse Fourier transform of the  $\phi$  component of the compensated image spectrum  $\tilde{I}'_c(m)$  is equal to the inverse Fourier transform of the total compensated image spectrum  $\tilde{I}'_c(m)$ . Therefore, it is sufficient to take the inverse Fourier transform of only the  $\phi$  component. Then, the resultant compensated image is a function

of  $\phi$  with  $\rho = r_2$ . This simplifies the loss compensation by reducing the post-processing to the calculation of only the  $\phi$  component.

### G. Selection of the cut off frequency for the transfer function

According to Eqs. (36) and (43), in the ideal case, the compensated image will recover all the information of the object. However, we acquire the transfer function and the image from finite element simulations. Noise corresponding to numerical error will be produced during the simulation because of the imperfect mesh size and solver settings in COMSOL. Due to the losses in the imaging process, the amplitude of high spatial frequency components become comparable or less than the noise at the image plane. This marks the cut off frequency. Here we define a variable  $\gamma$ :

$$\gamma = \max(A_i) / \min(A_i) \quad (46)$$

where  $A_i$  is the amplitude of the cylindrical wave at the image plane for the  $i$ th spatial frequency. The condition for the cut off frequency is determined by  $\gamma = 3dB$  below unless otherwise is stated. This means that we consider only the spatial frequency components less than the cut off frequency, for which  $\min(A_i) \geq 0.5 \max(A_i)$ . We refer to the resultant object which excludes high spatial frequencies above cut off as the "truncated object." In signal processing, 3dB attenuation commonly defines the cut off frequency for filters.

## 3. Applicability of the $\Pi$ scheme to different loss mechanisms in the imaging system

The major loss mechanisms responsible for deterioration of the hyperlens image resolution include absorption, inherently discretized unit cells, and impedance mismatch. In our previous work, it has been already shown that the  $\Pi$  scheme is capable of compensating the absorption loss in a homogeneous impedance matched negative index flat lens [46]. In contrast, the hyperlens considered in Ref. [47] was absorbing, consisting of discretized unit cells, and impedance mismatched. Using the  $\Pi$  scheme, we enhanced the resolution of such hyperlens from  $\lambda_0/4.5$  to  $\lambda_0/7$  (i.e., a factor of about 1.6 enhancement in the resolution). However, we did not distinguish what types of losses were compensated in the process. In this section, we will explicitly show that all of the above losses are accounted by the  $\Pi$  scheme.

### A. Absorption loss

To achieve our goal we start from an absorbing, inhomogeneous, and impedance mismatched experimental hyperlens studied in detail in Ref. [47] and re-described in Fig. 1. It is trivial to prove the compensation of the absorption loss with the  $\Pi$  scheme. When we remove the absorption loss from the hyperlens by defining the silver with  $\epsilon_m = -2.4012$  in the simulation, this immediately improves the resolution of the uncompensated hyperlens from  $\lambda_0/4.5$  to  $\lambda_0/5.4$ , indicating that the part of the compensation achieved initially in Ref. [47] was indeed for the absorption loss, which is not surprising as the original hyperlens was absorptive due to the non-zero imaginary part existing in the metal permittivity.

### B. Discretization loss

Since the hyperlens is a layered structure, the discretization can also lead to losses. We can consider a layered structure as an effective homogenous medium under the assumption that the layer thickness is much smaller than one effective wavelength  $\lambda_\rho$  along the radial direction. Based on Eq. (16), when the spatial frequency  $k_\phi$  is small (i.e., small  $m$  value), such that  $k_\rho$  is close to  $k_0$ , the regime where  $\lambda_\rho \sim \lambda_0$  is reached. However, in the case that the image contains small subwavelength features which correspond to large  $k_\phi$ ,  $k_\rho$  is much

larger than  $k_0$ . As a result,  $\lambda_p \ll \lambda_0$  and this leads to  $\lambda_p$  being comparable with the layer thickness. Thus, the effective medium assumption is no longer valid. The loss of information due to this process is identified as the discretization loss.

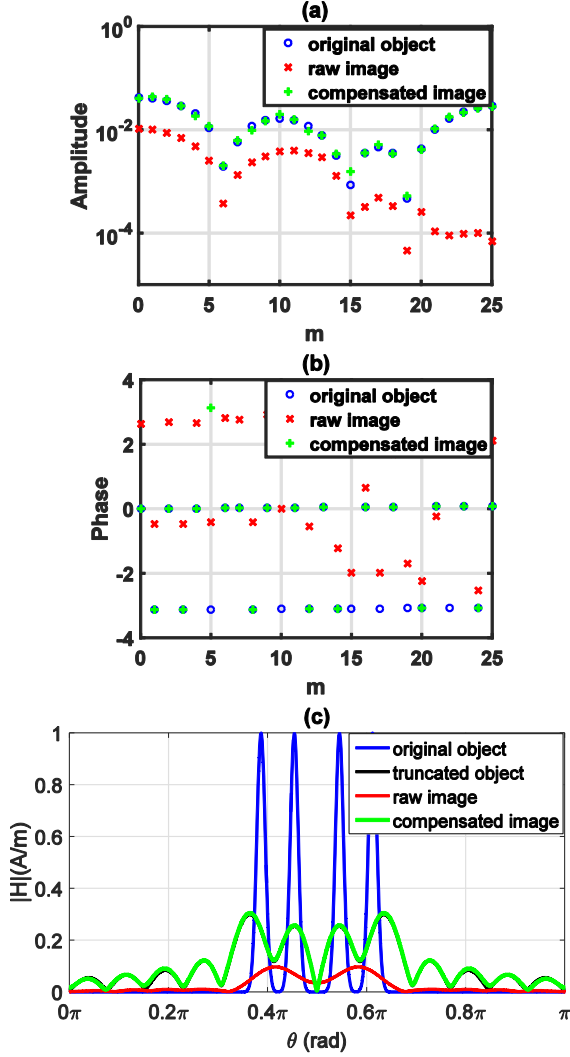


Figure 2. (a) Amplitude (A/m) and (b) phase Fourier spectra for the original object, raw image, and compensated image. (c) Magnetic field intensity for the original object, raw image and compensated image. The  $\Pi$  scheme accounts for the discretization and impedance mismatch losses resulting in a compensated image with a high resolution of  $\lambda_0/7$ .

Having eliminated the absorption loss by setting the imaginary part of the metal permittivity zero and applying the compensation procedure in section 2, the results are shown in Fig. 2. All the simulation details including object definitions can be found in Ref. [47]. Figs. 2 (a) and (b) show, respectively, the amplitude and phase information of the Fourier spectra of the original object [see Eq. (23)], the raw image [see Eq. (31)], and the compensated image [see Eq. (42)]. After the transformation into the spatial domain, the compensated image which corresponds to the green line is obtained in Fig. 2 (c) [see Eq. (45)]. It is clearly seen that the compensated image coincides with the truncated object (i.e., the object which excludes the high spatial frequencies beyond cut off) and reasonably well represents the original object with small subwavelength features separated by  $\lambda_0/7$ . This result indicates that the  $\Pi$  scheme compensates losses beyond the absorption loss.

### C. Impedance mismatch loss

Even though the enhancement factor due to the loss compensation in Fig. 2 and the direct removal of absorption and discretization above is the same (i.e.,  $\lambda_0/7$  resolution is obtained in both), this does not mean all the compensation in Fig. 2 are from the discretization. As we will show below, the impedance mismatch loss is another major loss mechanism and requires a definition of an object with a higher resolution in our analysis for a proof.

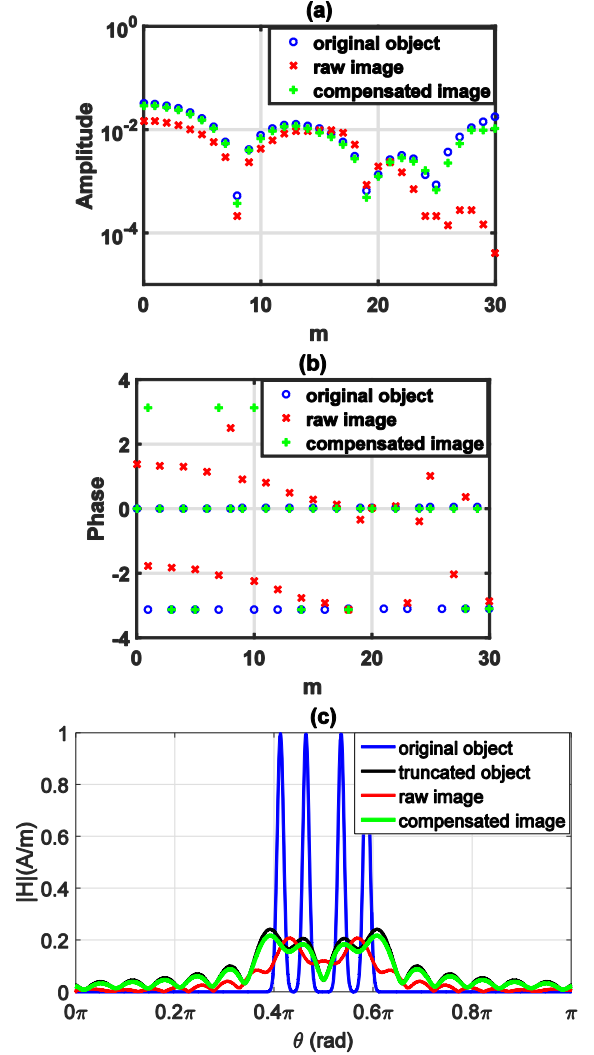


Figure 3. (a) Amplitude (A/m) and (b) phase Fourier spectra for the original object, raw image and compensated image. (c) Magnetic field intensity for the original object, raw image, and compensated image. The  $\Pi$  scheme accounts for impedance mismatch loss resulting in a compensated image with a high resolution of  $\lambda_0/9.6$ .

Therefore, to show the effect of loss compensation on the impedance mismatch, we reduced the object feature size to  $\lambda_0/9.6$ , so that the object cannot be resolved by the non-absorbing impedance mismatched hyperlens with 10nm layer thickness. Then, following the loss compensation procedure described in detail in section 2, we again applied the compensation filter to the raw image and obtained the loss compensated high resolution image, which is otherwise not possible without compensation. It should be noted that smaller the feature size is, larger the spatial frequency needed to reconstruct the object. If we still use  $\gamma = 3dB$  to determine the cut off frequency, which

corresponds to  $m = 26$ , the truncated object cannot well represent the four peaks in the original object, although the compensated image agrees well with the truncated object. Therefore, we increased the cut off to  $m = 30$ , which corresponds to  $\gamma = 5\text{dB}$ . The results are shown in Fig. 3. Figs. 3 (a) and (b) are the results in the Fourier domain and Fig. 3 (c) is the result in the spatial domain. It is clear that the  $\Pi$  scheme continues to compensate some other losses in the system despite negligible discretization loss and no absorption in the system.

When the electromagnetic waves impinge on the outer interface between the hyperlens and quartz substrate, the impedance inside the hyperlens is not matched with the impedance of the substrate (see Fig. 1). Note that since the objects are defined on the inner interface of the hyperlens, there is no impedance mismatch on the inner interface. We will show below that the impedance mismatch is another major loss mechanism, which is largely responsible from the remaining losses and the one compensated in Fig. 3.

The physical implementation of the  $\Pi$  scheme requires applying an auxiliary object coherently superimposed on the original object as the total object to obtain the resultant loss compensated high resolution image [42,46,47]. Considering this principle, first we calculate the equivalent auxiliary object from the  $\Pi$  scheme directly and then compare it with the auxiliary object calculated from impedance mismatch. If these two auxiliary objects are close to each other, it means the loss compensated in Fig. 3 mainly originates from impedance mismatch.

#### 1. Auxiliary object calculation from the $\Pi$ scheme directly

In the Fourier domain, the compensated image  $\tilde{I}_c(m)$  and the total object  $\tilde{O}_{total}(m)$  are related by the transfer function  $T(m)$  as:

$$\tilde{I}_c(m) = \tilde{O}_{total}(m)T(m) \quad (47)$$

The auxiliary object  $\tilde{O}_{aux}(m)$  satisfies the equation:

$$\tilde{O}_{aux}(m) = \tilde{O}_{total}(m) - \tilde{O}(m) \quad (48)$$

Then,  $\tilde{O}_{aux}(m)$  can be calculated by the equation:

$$\tilde{O}_{aux}(m) = \frac{\tilde{I}_c(m)}{T(m)} - \tilde{O}(m) \quad (49)$$

#### 2. Auxiliary object calculation from the impedance mismatch

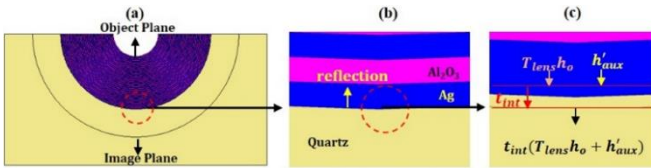


Figure 4. (a) A location where the impedance mismatch occurs. (b) The region indicated by the dashed circle in (a) is enlarged. (c) The region indicated by the dashed circle in (b) is enlarged. The two curves which are 2nm away from the interface are defined as the upper and the lower boundaries to calculate the transmission coefficient  $t_{int}(m)$ . See the text for the details.

The impedance mismatch appears at the interface between the hyperlens and the quartz substrate. As a result, some of the incident waves will reflect at the interface. The auxiliary object  $h'_{aux}(m)$  added at the interface will make the transmitted electromagnetic wave equal to the original incident wave. Fig. 4 shows the schematic for the calculation of the auxiliary object.

$h'_{aux}(m)$  satisfies the equation:

$$T_{lens}(m)h_o(m) = t_{int}(m)(T_{lens}(m) \cdot h_o(m) + h'_{aux}(m)) \quad (50)$$

where  $T_{lens}(m)$  is the transfer function from the object plane to the upper boundary,  $h_o(m)$  is the complex field described in section 2.D, and  $t_{int}(m)$  is the transmission coefficient at the interface.  $T_{lens}(m)$  and  $t_{int}(m)$  can be obtained by the similar calculations in section 2.D. After  $h'_{aux}(m)$  is obtained, the auxiliary object  $h_{aux}(m)$  that needs to be added at the object plane is equal to:

$$h_{aux}(m) = h'_{aux}(m)/T_{lens}(m) \quad (51)$$

#### 3. Comparison of the two auxiliary objects

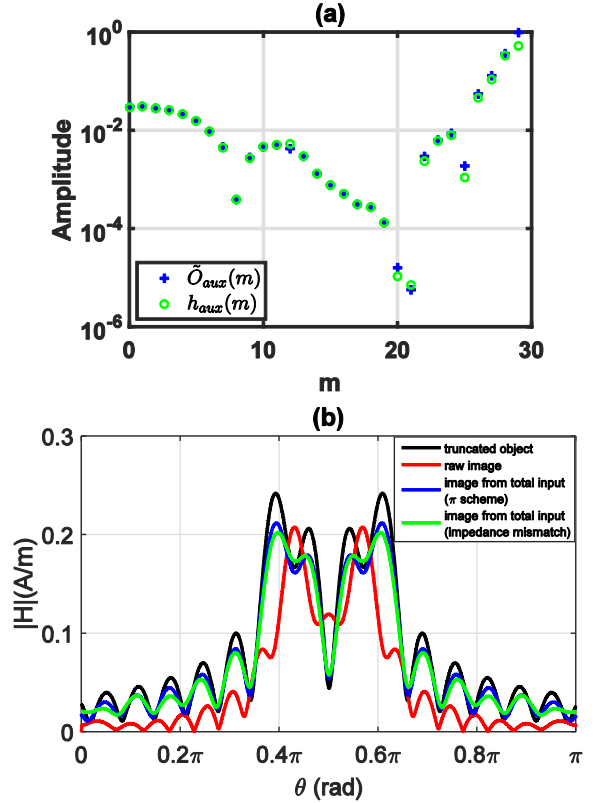


Figure 5. (a) Fourier spectra (A/m) for the auxiliary objects calculated by the two different methods. (b) Magnetic field intensity for the truncated object, raw image, and the image from the total input for the two different auxiliary objects.

$\tilde{O}_{aux}(m)$  and  $h_{aux}(m)$  calculated from Eqs. (49) and (51), respectively, are shown in Fig. 5. Fig. 5 (a) shows the Fourier spectra for the two auxiliary objects. After superimposing the auxiliary object on the original object, the corresponding image is obtained from the total input as shown in Fig. 5 (b). The blue curve in Figs. 5 (a) and (b) is obtained by using the auxiliary object calculated from the  $\Pi$  scheme directly as described in section 3.C.1, and the green curve is obtained from the impedance mismatch calculation as described in section 3.C.2. The results clearly show that the two auxiliary objects are quite close to each other. Therefore we can safely conclude that the origin of the losses compensated in Fig. 3 is mostly the impedance mismatch. Meanwhile, the results also indicate that the  $\Pi$  scheme is equivalent to mathematically applying a compensating inverse filter, which emulates the physical implementation of the scheme.



## 4. Discussion and Conclusion

It is interesting to compare the plasmon injection results for the hyperlens analyzed above in this paper and the planar plasmonic hyperlens (or “magnifying superlens”) considered in Refs. [34,35]. The latter consists of alternating layers of effective negative and positive refractive indices resulting from the SPP modes residing at the gold/polymethyl methacrylate and gold/vacuum interfaces, respectively. The plasmonic illumination is achieved by a phase-matching structure. The individual layer thicknesses inside the lens are adjusted such that the phase after propagation through each functional layer is restored to allow for ideal construction of the images. Such magnifying superlens has shown to resolve features of at least  $\lambda_0/7$ , which is comparable to that of loss compensated hyperlens analyzed in detail in this paper. However, we found that even the resolution of magnifying superlens can be further improved with the  $\Pi$  scheme. To verify this we performed simulations for the magnifying superlens and then applied plasmon injection inverse filter for possible enhancement in the image resolution. An object with Gaussian features that have intensity full-width-half-maximum (FWHM) of  $61\text{nm}$  were used in the simulations similar to the experiments [34,35]. The intensity FWHM for the Gaussian features in the resultant image was  $77\text{nm}$ , which was very close to the experimental results. With the plasmon injection inverse filter, the image contrast was improved and the FWHM was reduced by approximately 18%, hence resulting in improved resolution (see Fig. 6). The enhancement in resolution though was not as remarkable as in the hyperlens imaging system studied in detail above, because the magnifying superlens has not much room for improvement due to lesser losses and already sufficient performance for the given feature size. However, we have noticed that the  $\Pi$  scheme becomes more effective for enhancing the resolution of the magnifying superlens if smaller objects are imaged since those objects contain higher spatial frequencies which cannot be easily restored by the superlens alone anymore.

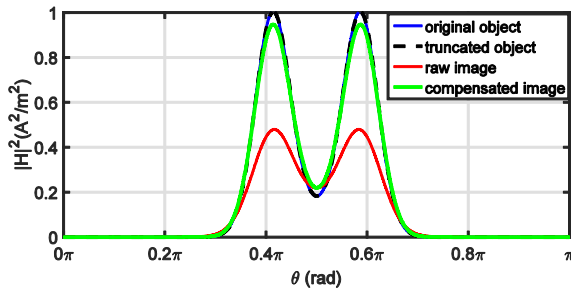


Figure 6. The image contrast and resolution of the magnifying superlens is improved with the plasmon injection inverse filter. The FWHM of the Gaussian features in the image is reduced from  $77\text{nm}$  (red solid line) to  $63\text{nm}$  (green solid line) with the plasmon injection inverse filter. The Gaussian features in the object has FWHM of  $61\text{nm}$  (blue solid line) and separated by  $130\text{nm}$ . The operating wavelength of the magnifying superlens is  $532\text{nm}$ . The truncated object (black dashed line) with  $m = 25$  perfectly represents the object in the filtering process.

To sum up, in this paper, the entire process of the inverse filter technique emulating the  $\Pi$  loss compensation scheme to boost the resolution of hyperlenses is described analytically in detail and implemented numerically using MATLAB and the finite element based COMSOL Multiphysics software package. It has been shown that the angular Fourier spectrum for the images obtained by the hyperlens is adequate for the mathematical implementation of the  $\Pi$  scheme. A strategy for determining the cut off frequency of the transfer function is discussed. Three major loss mechanisms responsible from the deterioration of the image resolution including absorption loss,

discretization loss, and impedance mismatch loss are identified and studied separately. The results demonstrate that all of these loss mechanisms existing in the imaging process can be compensated by the  $\Pi$  scheme and its inverse filter analogue. Finally, it should be noted that the possibility of compensating the discretization loss raises the hopes for overcoming the unit cell size limitation which determines the ultimate quality of the metamaterials (e.g., resolution of a metamaterial lens). This could relax the fabrication constraints by allowing for larger unit cell structures at a fixed operating wavelength.

**Funding Information.** Office of Naval Research (award N00014-15-1-2684).

## References

1. E. Abbe, “Beiträge zur Theorie des Mikroskops und der mikroskopischen Wahrnehmung,” *Arch. f. Mikr. Anat.* **9**, 413–420 (1873).
2. P. Genevet, F. Capasso, F. Aieta, M. Khorasaninejad, and R. Devlin, “Recent advances in planar optics: from plasmonic to dielectric metasurfaces,” *Optica* **4**, 139 (2017).
3. M. A. Al Farooqui, J. Breeland, M. I. Aslam, M. Sadatgol, S. K. Ozdemir, M. Tame, L. Yang, and D. O. Guney, “Quantum entanglement distillation with metamaterials,” *Opt. Express* **23** 17941 (2015).
4. M. Asano, M. Bechu, M. Tame, S. K. Ozdemir, R. Ikuta, D. O. Guney, T. Yamamoto, L. Yang, M. Wegener, and N. Imoto, “Distillation of photon entanglement using a plasmonic metamaterial,” *Sci. Rep.* **5** 18313 (2015).
5. P. K. Jha, X. Ni, C. Wu, Y. Wang, and X. Zhang, “Metasurface-enabled remote quantum interference,” *Phys. Rev. Lett.* **115** 025501 (2015).
6. J. Gwamuri, D. Ö. Güney, and J. M. Pearce, Advances in Plasmonic Light Trapping in Thin-Film Solar Photovoltaic Devices, in *Solar Cell Nanotechnology*, A. Tiwari, R. Boukherroub, and Maheshwar Sharon Eds. (John Wiley & Sons, 2013), pp. 241–269.
7. C. Rockstuhl, S. Fahr, and F. Lederer, “Absorption enhancement in solar cells by localized plasmon polaritons,” *J. Appl. Phys.* **104**, 123102 (2008).
8. A. Vora, J. Gwamuri, N. Pala, A. Kulkarni, J. M. Pearce, and D. O. Guney, Exchanging ohmic losses in metamaterial absorbers with useful optical absorption for photovoltaics,” *Sci. Rep.* **4**, 4901 (2014).
9. J. Valentine, S. Zhang, T. Zentgraf, E. Ulin-Avila, D. A. Genov, G. Bartal, and X. Zhang, “Three-dimensional optical metamaterial with a negative refractive index,” *Nature* **455**, 376 (2008).
10. N. I. Landy, S. Sajuyigbe, J. J. Mock, D. R. Smith, and W. J. Padilla, “Perfect metamaterial absorber,” *Phys. Rev. Lett.* **100**, 207402 (2008).
11. V. V. Temnov, “Ultrafast acousto-magneto-plasmonics,” *Nat. Photon.* **6**, 728 (2012).
12. M. I. Aslam and D. O. Guney, “On negative index metamaterial spacers and their unusual optical properties,” *Prog. Electromagn. Res. B* **47**, 203 (2013).
13. M. Sadatgol, M. Rahman, E. Forati, M. Levy, and D. O. Guney, “Enhanced Faraday rotation in hybrid magneto-optical metamaterial structure of bismuth-substituted-iron-garnet with embedded-gold-wires,” *J. Appl. Phys.* **119**, 103105 (2016).
14. M. Choi, S. H. Lee, Y. Kim, S. B. Kang, J. Shin, M. H. Kwak, K.-Y. Kang, Y.-H. Lee, N. Park, and B. Min, “A terahertz metamaterial with unnaturally high refractive index,” *Nature* **470**, 369, (2011).
15. W.-C. Chen, C. M. Bingham, K. M. Mak, N. W. Caira, and W. J. Padilla, “Extremely sub-wavelength planar magnetic metamaterials,” *Phys. Rev. B* **85**, 201104 (2012).
16. X. Zhang, E. Usi, S. K. Khan, M. Sadatgol, and D. O. Guney, “Extremely subwavelength negative index metamaterial,” *Progress in Electromagnetic Research* **152**, 95 (2015).
17. D. Schurig, J. J. Mock, B. J. Justice, S. A. Cummer, J. B. Pendry, A. F. Starr, and D. R. Smith, “Metamaterial electromagnetic cloak at microwave frequencies,” *Science* **314**, 977 (2006).



18. D. O. Güney and D. A. Meyer, "Negative refraction gives rise to the Klein Paradox," *Phys. Rev. A* **79**, 063834 (2009).
19. J. B. Pendry, "Negative refraction makes a perfect lens," *Phys. Rev. Lett.* **85**, 3966 (2000).
20. R. A. Shelby, D. R. Smith, and S. Schultz, "Experimental Verification of a Negative Index of Refraction," *Science* **292**, 77 (2001).
21. D. R. Smith, D. Schurig, M. Rosenbluth, and S. Schultz, "Limitations on subdiffraction imaging with a negative refractive index slab," *Appl. Phys. Lett.* **82**, 1506 (2003).
22. N. Fang, H. Lee, C. Sun, and X. Zhang, "Sub-diffraction-limited optical imaging with a silver superlens," *Science* **308**, 534 (2005).
23. T. Taubner, D. Korobkin, Y. Urzhumov, G. Shvets and R. Hillenbrand, "Near-Field Microscopy Through a SiC Superlens," *Science* **313**, 1595 (2006).
24. X. Zhang and Z. Liu, "Superlenses to overcome the diffraction limit," *Nature Mater.* **7**, 435 (2008).
25. T. Xu, A. Agrawal, M. Abashin, K. J. Chau, and H. J. Lezec, "All-angle negative refraction and active flat lensing of ultraviolet light," *Nature* **497**, 470 (2013).
26. R. Maas, J. van de Groep, and A. Polman, "Planar metal/dielectric single-periodic multilayer flat lens," *Optica* **3**, 592 (2016).
27. Z. Jacob, L. V. Alekseyev, and E. E. Narimanov, "Optical hyperlens: far-field imaging beyond the diffraction limit," *Opt. Express* **14**, 8247 (2006).
28. B. Wood and J. B. Pendry, "Directed sub-wavelength imaging using a layered metal-dielectric system," *Phys. Rev. B* **74**, 115116 (2006).
29. J. Z. Liu, H. Lee, Y. Xiong, C. Sun, and X. Zhang, "Far-field optical hyperlens magnifying sub-diffraction-limited objects," *Science* **315**, 1686 (2007).
30. J. Rho, Z. Ye, Y. Xiong, X. Yin, Z. Liu, H. Choi, G. Bartal, and X. Zhang, "Spherical hyperlens for two-dimensional sub-diffractional imaging at visible frequencies," *Nature Commun.* **1**, 143 (2010).
31. D. Lu and Z. Liu, "Hyperlenses and metalenses for far-field super-resolution imaging," *Nat. Commun.* **3**, 1205 (2012).
32. J. Sun, M. Shalaev, and N. Litchinitser, "Experimental demonstration of a non-resonant hyperlens in the visible spectral range," *Nature Commun.* **6**, 7201 (2015).
33. H. Lee, Z. Liu, Y. Xiong, C. Sun, and X. Zhang, "Development of optical hyperlens for imaging below the diffraction limit," *Opt. Express* **15**, 15886 (2007).
34. I. I. Smolyaninov, Y.-J. Hung, and C. C. Davis, "Magnifying superlens in the visible frequency range," *Science* **315**, 1699 (2007).
35. I. I. Smolyaninov, Y.-J. Hung, and C. C. Davis, "Imaging and focusing properties of plasmonic metamaterial devices," *Phys. Rev. B* **76**, 205424 (2007).
36. W. Adams, M. Sadatgol, and D. O. Güney, "Review of near-field optics and superlenses for sub-diffraction-limited nano-imaging," *AIP Advances* **6**, 100701 (2016).
37. B. Yan, Z. Wang, A. Parker, Y. Lai, J. Thomas, L. Yue, and J. Monks, "Superlensing microscope objective lens," *arXiv: 1611.00077*.
38. Z. Wang, "Microsphere super-resolution imaging," *Nanoscience* **3**, 193 (2016).
39. D. O. Güney, Th. Koschny, and C. M. Soukoulis, "Reducing ohmic losses in metamaterials by geometric tailoring," *Phys. Rev. B* **80**, 125129 (2009).
40. T. Koschny, P. Markoš, E. N. Economou, D. R. Smith, D. C. Vier, and C. M. Soukoulis, "Impact of inherent periodic structure on effective medium description of left-handed and related metamaterials," *Phys. Rev. B* **71**, 245105 (2005).
41. A. Kildishev and E. E. Narimanov, "Impedance-matched hyperlens," *Opt. Lett.* **32**, 3432 (2007).
42. M. Sadatgol, S. K. Ozdemir, L. Yang, and D. O. Güney, "Plasmon injection to compensate and control losses in negative index metamaterials," *Phys. Rev. Lett.* **115**, 35502 (2015).
43. D. O. Güney, Th. Koschny, and C. M. Soukoulis, "Surface plasmon driven electric and magnetic resonators for metamaterials," *Phys. Rev. B* **83**, 045107 (2011).
44. M. I. Aslam and D. O. Güney, "Surface plasmon driven scalable low-loss negative-index metamaterial in the visible spectrum," *Phys. Rev. B* **84**, 195465 (2011).
45. M. I. Aslam and D. O. Güney, "Dual band double-negative polarization independent metamaterial for the visible spectrum," *J. Opt. Soc. Am. B* **29**, 2839 (2012).
46. W. Adams, M. Sadatgol, X. Zhang, and D. O. Güney, "Bringing the 'perfect lens' into focus by near-perfect compensation of losses without gain media," *New Journal of Physics* **18**, 125004 (2016).
47. X. Zhang, W. Adams, M. Sadatgol, and D. O. Güney, "Enhancing the resolution of hyperlens by the compensation of losses without gain media," *Progress in Electromagnetic Research C* **70**, 1 (2016).
48. E. J. Betzig and J. K. Trautman, "Breaking the diffraction barrier: optical microscopy on a nanometric scale," *Science* **251**, 1468 (1991).
49. J. K. Trautman, E. Betzig, J. S. Weiner, D. J. DiGiovanni, T. D. Harris, F. Hellman, and E. M. Gyorgy, "Image contrast in near-field optics," *J. Appl. Phys.* **71**, 4659 (1992).
50. H. Hatano and S. Kawata, "Applicability of deconvolution and nonlinear optimization for reconstructing optical images from near-field optical microscope images," *J. Microsc.* **194**, 230 (1999).
51. F. Kiendl and G. Güntherodt, "Computational methods to produce enhanced images out of given SNOM raw data," *Ultramicroscopy* **102**, 299 (2005).
52. G. Derveaux, G. Papanicolaou, and C. Tsogka, "Resolution and denoising in near-field imaging," *Inverse Problems* **22**, 1437 (2006).
53. C. A. Balanis, *Advanced Engineering Electromagnetics*, (2012).
54. S. S. Kruk, D. A. Powell, A. Minovich, D. N. Neshev, and Y. S. Kivshar, "Spatial dispersion of multilayer fishnet metamaterials," *Opt. Express* **20**, 15100 (2012).
55. X. Zhang, S. Debnath, and D. O. Güney, "Hyperbolic metamaterial feasible for fabrication with direct laser writing processes," *J. Opt. Soc. Am. B* **32**, 1013 (2015).